Magnetic properties of $CeRh_3B_2$ investigated by muon spin rotation spectroscopy

F. N. Gygax and A. Schenck
Institute for Particle Physics of ETH Zurich (IPP), CH-5232 Villigen PSI, Switzerland

Y. Ōnuki
Faculty of Science, Osaka University, Machikaneyama, Toyonaka, Osaka 560, Japan

Ch. Reichl* and G. Wiesinger
Institute for Solid State Physics, Vienna University of Technology, A-1040 Vienna, Austria
(Received 28 June 2005; revised manuscript received 4 November 2005; published 20 April 2006)

We report on positive muon spin rotation (μ^+SR) measurements on hexagonal $CeRh_3B_2$ single crystals. This ferromagnetic material, with the high Curie temperature of $T_C \approx 120$ K, shows anomalous magnetic properties. In the magnetically ordered state, two spontaneous μ^+-precession frequencies are observed in zero applied magnetic field. The peculiar temperature dependence of these frequencies shows that a magnetization is found on Ce *and*, over a wide temperature range, on the Rh atoms. There is a strong indication that a significant negative fraction of the magnetization connected to the Ce atoms is delocalized on the *c*-axis Ce-Ce chains. The analysis renders it necessary to allow for an unusual temperature dependence of the Rh-sublattice magnetization, deviating significantly from the Ce-sublattice magnetization. This points to a temperature dependent exchange coupling between the Ce and Rh 4*f* and 4*d* states. Transverse-field measurements above T_C allow one to specify the interstitial sites occupied by the muons and indicate the presence of long-range μ^+ diffusion for $T > 125$ K.

DOI: 10.1103/PhysRevB.73.144423 PACS number(s): 75.50.Cc, 75.30.Cr, 76.60.Cq, 76.75.+i

I. INTRODUCTION

$CeRh_3B_2$, with a hexagonal $CaCu_5$-type crystal structure (space group $P6/mmm$ no. 191), shows anomalous ferromagnetic properties. The observed Curie temperature $T_C \approx 120$ K is the highest value of all the cerium compounds and exceeds by two orders of magnitude the ordering temperature expected on the basis of the de Gennes factor. The saturation magnetic moments of 0.45 μ_B at 2 K are found to lie in the basal plane, preferably aligned along the $[10\bar{1}0]$ direction, as discussed by Galatanu *et al.*[1] According to these authors, the possibility of a simple localized picture for the $CeRh_3B_2$ magnetism is ruled out, even when crystal electric field (CEF) effects are taken into account. Itinerant magnetism may play a rôle in relation to the very high T_C value, however, another explanation involving an additional quadrupolar ordering mechanism has also been conjectured.[1]

Nuclear magnetic resonance (NMR)[2] and other experiments[3–5] indicate that there are only negligible magnetic moments on the Rh and B sites. A polarized neutron scattering study[6] performed at 7 K has determined that the magnetic moment of the cerium ion is $\mu_{Ce}=\mu_{4f}+\mu_{5d}=0.38$ μ_B, with $\mu_{4f}=+0.56$ μ_B and $\mu_{5d}=-0.18$ μ_B. The strongly anisotropic 5*d* density arises from hybridization of Ce-4*f* electrons with conduction electrons. These results, however, are not unchallenged. With their alternative analysis, apparently also based on the neutron scattering measurement later reported in Ref. 6, Kasuya *et al.*[7] arrive at different conclusions. They give for the moment on the Ce site a value of 0.84 μ_B/Ce, and they find a moment of -0.09 μ_B/Rh at the Rh site, which yields a total moment of 0.57 μ_B/f.u. The saturation magnetization obtained in the polarized neutron study, 0.38 or 0.42 μ_B, depending on the analysis,[6] is close but not exactly equal to the presently recognized value[1] of 0.45 μ_B. In any case, the μ_{Ce} value is small compared to the usual values for Ce ions in magnetically ordered compounds. Magnetic-Compton-scattering (MCS) studies[8,9] have been performed to measure the *electron spin* magnetic moments, and it is found[8] that the Kondo effect does not play a key rôle in the mechanism leading to the extraordinary T_C value. A definitive explanation for this value is still lacking.

In the paramagnetic phase, the magnetic susceptibility shows a Curie-Weiss (CW) behavior only above 400 K for $\boldsymbol{H}$ in the basal plane, and only above 600 K for $\boldsymbol{H} \| [0001]$, yielding effective magnetic moments of 2.9 and 2.3 μ_B, respectively.[1] These values are close to the theoretical value $\mu_{eff}=2.54$ μ_B for the free Ce^{3+} ion. The paramagnetic Curie temperatures from the CW-relation fits are large and negative.

A de Haas-van Alphen study has revealed a unique quasi-one dimensional character of the Fermi surface.[10] The wavy but flat Fermi surface in the basal plane, mainly due to a well-hybridized band of Rh-4*d* and B-2*p* electrons, is thought to reflect the very short lattice parameter $c = 3.087$ Å in $CeRh_3B_2$, in contrast to all other intermetallic Ce compounds. By comparison, the *a* parameter has the more "normal" value of 5.484 Å. As opposed to the case of isostructural $PrRh_3B_2$, for $CeRh_3B_2$ only a *tentative* CEF scheme has yet been proposed.[11]

With muon-spin rotation and relaxation spectroscopy (μSR) we have observed that in $CeRhIn_5$ (Ref. 12) and Ce_2RhIn_8,[13] contrary to expectations, also the Rh sublattice develops ordered magnetic moments. This has prompted us to examine other Rh-containing Ce compounds. Thus, we report here on μ^+SR measurements on $CeRh_3B_2$ single crystals performed in zero-field (ZF) and transverse-field (TF)

configurations, revealing again that the Rh 4*d* electrons take part in the magnetic order. The present results and interpretation differ from the study of polycrystalline $CeRh_3B_2$ reported by Cooke *et al.*[14]

II. EXPERIMENTAL DETAILS

The μSR measurements were performed at the Swiss Muon Source of the Paul Scherrer Institut (PSI), using the general purpose spectrometers "GPS" and "Dolly." Both instruments are supplied with surface μ^+ with essentially 100% spin polarization and 4 MeV kinetic energy. They allow one to monitor the decay positrons from the μ^+ implanted into the sample using five positron detectors placed in the forward (F), backward (B), up (U), down (D), and right (R) directions with respect to the μ^+ beam momentum. The beam lines are equipped with spin rotators, enabling the polarization of the incoming μ^+ (with spin initially pointing backwards) to be rotated by up to $\sim 50°$ towards the vertical (up) direction. With an external field applied along the beam direction, this feature allows one to perform a transverse-field (TF) measurement (using the U, D, and R detectors) in parallel with a longitudinal-field (LF) measurement (using the F and B detectors). A comprehensive description of the spectrometers and muon-beam characteristics can be found in Ref. 15.

Two $CeRh_3B_2$ single crystals were prepared at Osaka University, and details are reported in Ref. 10. The quality of the samples has appreciably evolved in time, as documented, e.g., by the Curie temperature: $T_C = 112$ K in 1985,[2] 115 K in 1988,[16] and now $T_C = 120.8$ K for the Osaka crystals.[1] A first crystal had the approximate shape of a half disk, with diameter ~ 4 mm and thickness ~ 1.5 mm. The second crystal, approximately a parallelepiped $3.5 \times 1.3 \times 1.1$ mm^3, was previously used in de Haas-van Alphen measurements.[10] Its crystallographic *c* axis, i.e., [0001], is parallel to the longest edge, and $[11\bar{2}0]$ is parallel to the shortest edge. This second sample, which was used in the GPS instrument, could be rotated about its $[10\bar{1}0]$ axis, which was oriented perpendicular to the beam and to the applied field. Hence the initial polarization $\boldsymbol{P}_\mu(t=0)$ or $\boldsymbol{H}_{\text{ext}}$ could be scanned in the $(10\bar{1}0)$ plane. To minimize the μSR signal not originating from the $CeRh_3B_2$ crystal, the sample, mounted in a helium-flow cryostat, was supported at the end of the sample holder solely by Mylar tape. A third single crystal, from the same batch as that used for the Grenoble neutron study,[6] has also been examined with the zero-field (ZF) μSR technique at the GPS spectrometer. This sample, grown with pure ^{11}B, was previously used for the high-energy MCS study.[8] Its shape is that of a plate approximately $1.5 \times 4 \times 6$ mm^3, with the $[11\bar{2}0]$ axis perpendicular to the sample plane.

In a μSR experiment, the evolution of the μ^+ polarization $\boldsymbol{P}_\mu(t)$ is monitored via the time-dependent decay asymmetry of the implanted μ^+ by observing the positrons from the μ^+ decay in a certain direction $\boldsymbol{r}$ as a function of elapsed μ^+ lifetime. The positron rate can then be written as[17]

$$\frac{dN_{e^+}(t)}{dt} = \frac{1}{4\pi\tau_\mu} N_0 e^{-t/\tau_\mu}[1 - A\boldsymbol{P}_\mu(t)\cdot\boldsymbol{r}]d\Omega_r, \qquad (1)$$

where A is the effective decay asymmetry (0.2–0.3), τ_μ the mean muon lifetime (2.197 μs), $|\boldsymbol{r}| = 1$, and $d\Omega_r$ is a solid angle element in the direction of $\boldsymbol{r}$. The product $AP_\mu(0) \equiv A\boldsymbol{P}_\mu(0)\cdot\boldsymbol{r}$ is often called the asymmetry or the signal amplitude. A μ^+ experiencing a local magnetic field $\boldsymbol{B}$ performs a Larmor precession about $\boldsymbol{B}$ with the frequency

$$\omega \equiv 2\pi\nu = \gamma_\mu|\boldsymbol{B}|. \qquad (2)$$

γ_μ, the μ^+ gyromagnetic ratio, is given by $\gamma_\mu = 2\pi \times 13.554$ MHz kG^{-1}.

III. TF MEASUREMENTS

Transverse-field measurements were primarily performed on $CeRh_3B_2$ in the paramagnetic state to determine the μ^+ site or sites from the μ^+ Knight shift by the standard procedure.[18] In general, TF measurements yield one or more μ^+ precession frequencies shifted and/or split in comparison with the precession frequency corresponding to the undisturbed applied field. The shifts are due to the additional internal magnetic fields at the muon locations.

The TF muon precession was measured in an applied field $\boldsymbol{H}_{\text{ext}}$, $H_{\text{ext}} = 6$ kOe, for various $CeRh_3B_2$ crystal orientations in the field, and as a function of temperature with 120 K $\leqslant T \leqslant$ 300 K. The data reveal a single-component signal with an anisotropic frequency shift. A thorough examination with the usual methods such as Fourier transforms and free multicomponent fits do not indicate a signal splitting. The μSR signal is fitted with a Gaussian relaxation function of the form

$$AP(t) = Ae^{-\sigma^2 t^2/2}\cos(\omega t + \phi). \qquad (3)$$

[An exponential relaxation function, $P(t) \propto e^{-\lambda t}$, gives fits of equivalent quality for $T = 125$ K, and above that temperature it fits the data even better. Both fits, with Gaussian- or exponential-relaxation functions, yield practically identical frequencies.] The signal amplitude corresponds to the maximum amplitude obtained with the chosen spectrometer settings, i.e., no missing polarization is detected. As an example, for $T = 125$ K, Fig. 1 shows the frequency shift $[(\omega - \gamma_\mu H_{\text{ext}})/(\gamma_\mu H_{\text{ext}})]$ as a function of the angle Θ between the applied field and the crystallographic [0001] axis, with $\boldsymbol{H}_{\text{ext}}$ confined to the $(10\bar{1}0)$ plane. The temperature dependencies of the μ^+ frequency for $\boldsymbol{H}_{\text{ext}}$ either parallel to the crystallographic *c* axis ($\boldsymbol{H}\|[0001]$) or parallel to $[11\bar{2}0]$ or $[10\bar{1}0]$ were also obtained. A small but clearly negative frequency shift is observed for $\boldsymbol{H}\|[11\bar{2}0]$ and $\boldsymbol{H}\|[10\bar{1}0]$, whereas the shift is nearly zero (slightly positive at the lowest temperatures) for $\boldsymbol{H}\|[0001]$.

Together with the anisotropic and *T*-dependent *frequency* of the TF μSR signal, a varying *relaxation rate* σ [Eq. (3)] or λ is also observed. For example, an anisotropic σ is seen for the frequency signal of Fig. 1, at 125 K. That is, the variation of the angular dependence of σ^2 is approximately described by a $\cos^2(\Theta)$ function; σ has a maximum of 0.55(3) μs^{-1} for $\boldsymbol{H}\|\boldsymbol{c}$, and a minimum of 0.21(3) μs^{-1} for $\boldsymbol{H} \perp \boldsymbol{c}$. For an assumed μ^+ site in the crystal, one can calculate the second moment M_2 of the field distribution arising from the surrounding randomly oriented nuclear dipole moments (the relaxation rate is then $\sigma = \sqrt{M_2}$). In $CeRh_3B_2$ the relevant di-

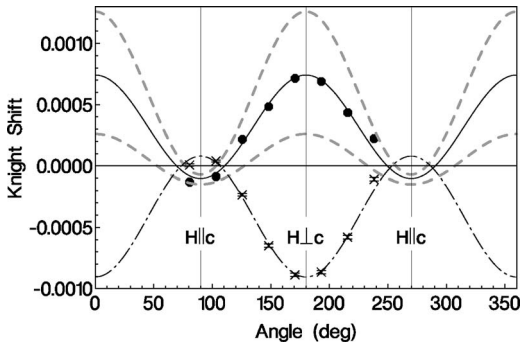

FIG. 1. Crystal-orientation dependence of the unique TF-μSR frequency shift in $CeRh_3B_2$ at 125 K. The crystal is rotated about its $[10\bar{1}0]$ axis, which is kept perpendicular to $\boldsymbol{H}_{\mathrm{ext}}$. The abscissa parameter is $\Theta+90°$, with Θ the angle between the applied field and the crystallographic c axis. $\times$: Raw frequency-shift data, • : Knight-shift data after demagnetization- and Lorentz-field corrections. Dash-dotted and full curves: $\cos^2(\Theta)$ fits to the raw and corrected data points, respectively. The dashed curves indicate limits of the maximum possible systematic errors in the Knight shift due to demagnetization-correction uncertainties.

poles are those of the ^{11}B nuclei; the natural abundance of this isotope being 81%. The expected angular dependence of M_2 should be described by a $P_4(\cos\Theta)$ term, where P_n are the Legendre polynomials. The actually observed angular dependence points to contributions from inhomogeneous demagnetization fields and is, therefore, smoother than the $\cos^4$ term in the $P_4(\cos\Theta)$ polynomial. A discussion of the signal relaxation is deferred to Sec. III D.

A. Observed μ^+ Knight shift K_μ

To obtain the Knight shifts from the shifts of the precession frequencies, one has to correct for demagnetization and Lorentz fields, which necessitates the knowledge of the bulk magnetic susceptibility $\boldsymbol{\chi}$ of the sample. The Lorentz field is just proportional to the bulk magnetization $\boldsymbol{M}=\boldsymbol{\chi}\boldsymbol{H}_{\mathrm{ext}}$, $\boldsymbol{B}^{\mathrm{Lor}}=+(4\pi/3)\boldsymbol{M}$. The demagnetization field $\boldsymbol{B}^{\mathrm{dem}}$ is calculated using the demagnetization tensor $\mathbf{N}$; that is, $\boldsymbol{B}^{\mathrm{dem}}=-4\pi\mathbf{N}\boldsymbol{M}$. The temperature dependence of $\boldsymbol{\chi}$ shows a large anisotropy.[1] For $\boldsymbol{H}\|[11\bar{2}0]$ and $\boldsymbol{H}\|[10\bar{1}0]$, the susceptibilities $\chi_{[11\bar{2}0]}(T)$ and $\chi_{[10\bar{1}0]}(T)$ are practically identical and they follow a Curie-Weiss law only above 400 K. For $\boldsymbol{H}\|\boldsymbol{c}$, $\chi_{[0001]}(T)$ is smaller than $\chi_{[11\bar{2}0]}(T)\approx\chi_{[10\bar{1}0]}(T)$ and shows the CW behavior only above 600 K. (In Ref. 1 a difference of 1% to 2% is found between $\chi_{[11\bar{2}0]}$ and $\chi_{[10\bar{1}0]}$, which is believed to be significant, particularly in the ordered state of $CeRh_3B_2$. In our analysis, such a difference plays no rôle and we disregard it.) Since the shape of the sample is not an ellipsoid, the demagnetization field will be inhomogeneous.

The correction procedure can be illustrated, for instance, for $\boldsymbol{H}_{\mathrm{ext}}$ along the principal axes of the crystal. The Knight-shift components are deduced from the frequency shifts using[18]

$$K_i=\frac{\nu_i-\nu_0}{\nu_0}-4\pi\left(\frac{1}{3}-N_\alpha\right)\chi_i, \tag{4}$$

where the index i distinguishes the cases $\boldsymbol{H}_{\mathrm{ext}}\|[11\bar{2}0]$, $\boldsymbol{H}_{\mathrm{ext}}\|[10\bar{1}0]$, and $\boldsymbol{H}_{\mathrm{ext}}\|[0001]$, respectively. The N_α are the average demagnetization factors of the parallelepiped-shaped sample (here with one of the sample axes, specified by the index α, parallel to $\boldsymbol{H}_{\mathrm{ext}}$). These demagnetization factors are estimated using tabulated values for rectangular box samples.[19] As can be seen in Fig. 1, the combined demagnetization and Lorentz field corrections are quite important. The asymmetry of the Θ dependence of the raw frequency shift, well fitted by a $\cos^2(\Theta)$ function, changes sign to describe the corrected Knight shift. The corrections (and their systematic errors) are important essentially where the susceptibility is important, i.e., for $\boldsymbol{H}\perp\boldsymbol{c}$. The precision of the demagnetization correction is sensitive to the exact sample alignment in the field and, mainly, to the estimated demagnetization factors. The latter imply residual uncertainties due to the interpolation steps needed between the tabulated values.[19] Both effects have been considered, therefore, by performing a series of correction evaluations, taking various overestimated *systematic* errors for the demagnetization factors. Examples are presented in Table I.

The extreme envelope of the results is indicated in Fig. 1 by the two dashed curves bracketing the Knight shifts corresponding to the nominal corrections. Although the maximum possible systematic error can be important, the signs of the Knight shifts for $\boldsymbol{H}\perp\boldsymbol{c}$ and $\boldsymbol{H}\|\boldsymbol{c}$ are clearly defined, the additional statistical errors of the frequency shifts being very small. The temperature dependencies of the correspondingly corrected Knight shifts for the three principal crystal orientations are shown in Fig. 2.

B. Scaling of K_μ with the magnetic susceptibility

The observation of a single-component Knight-shift signal indicates that the μ^+ occupy a single type of crystallographic site, with identical local fields, both in magnitude and in direction for a given orientation of the crystal relative to $\boldsymbol{H}_{\mathrm{ext}}$. This implies a site where the sum of the dipolar fields of the surrounding moments is described by a tensor with axial symmetry (in short: A site with an axially symmetric dipolar field). However, this Knight-shift could also result from μ^+ occupying *two different crystallographic sites with*, by chance, *almost identical axially symmetric dipolar fields*.

The unit cell of hexagonal $CeRh_3B_2$ is shown in Fig. 3. Ce occupies the 1a site, position $(0,0,0)$, Rh the 3g sites, generic position $(\frac{1}{2},0,\frac{1}{2})$, and B is found at the 2c sites, generic position $(\frac{1}{3},\frac{2}{3},0)$. For this structure, assuming that only the Ce ions carry magnetic moments, the dipolar field is easily calculated for the paramagnetic phase. The only sites with a field showing axial symmetry are either the 2e sites on the c axis connecting two Ce ions (including the particular centered 1b site) or the 4h sites on an axis parallel to $\boldsymbol{c}$ connecting two B atoms (including the centered 2d sites). (This conclusion remains valid if magnetic densities are also found on the Rh atoms or on the c axis linking the Ce ions.)

In general, one assumes that the Knight shift consists of two contributions: A dipolar-field term and a contact-hyperfine term. The dipolar field originates from the moments induced by the external field $\boldsymbol{H}_{\mathrm{ext}}$, and the contact term arises from the spin polarization of the conduction electrons at the μ^+ site. The spin polarization is predominantly caused

TABLE I. Determination of the combined demagnetization- and Lorentz-field corrections for the TF measurements, $\Delta_i^{\mathrm{corr}}=-4\pi\left(\frac{1}{3}-N_\alpha\right)\chi_i$ [compare Eq. (4)]. Examples are given for the three principal sample orientations in the external field at $T=125$ K. For each orientation the demagnetization factor N_α is considered at its nominal value and at the lowest and highest values assumed for the extreme systematic deviations. ρ_m is the molar density of $CeRh_3B_2$.

Orientation i		N_α	$-4\pi\left(\frac{1}{3}-N_\alpha\right)\rho_m$ (mol/emu)	χ_i/ρ_m (emu/mol)	$\frac{\nu_i-\nu_0}{\nu_0}$ [a]	Δ_i^{corr}	K_i [a]
[0001]	($\boldsymbol{H}\parallel\boldsymbol{c}$)	0.130	−0.0528	4.02×10^{-3}	0.000 08(1)	−0.000 22	−0.000 15(1)
		0.158	−0.0455			−0.000 18	−0.000 10(1)
		0.190	−0.0372			−0.000 15	−0.000 07(1)
[11$\bar{2}$0]	($\boldsymbol{H}\perp\boldsymbol{c}$)	0.45	0.0303	3.82×10^{-2}	−0.000 90(2)	0.001 16	0.000 26(2)
		0.50	0.0433			0.001 65	0.000 75(2)
		0.55	0.0562			0.002 15	0.001 26(2)
[10$\bar{1}$0]	($\boldsymbol{H}\perp\boldsymbol{c}$)	0.39	0.0147	3.85×10^{-2}		0.000 57	
		0.44	0.0277			0.001 07	
		0.49	0.0407			0.001 57	

[a]Values of Fig. 1, statistical errors in parentheses.

via the Rudermann–Kittel–Kasuya–Yosida (RKKY) mechanism by the moments induced in the $4f$ shell of Ce^{3+} and should scale with the magnetic susceptibility. As usual we may write[18]

$$K_\kappa=(A^{\mathrm{c}}+A_{\kappa\kappa}^{\mathrm{dip}})\chi_\kappa+K_\kappa^0,\quad \text{with } \kappa=[11\bar{2}0],[10\bar{1}0],[0001]. \tag{5}$$

A^{c} is the contact-coupling constant, assumed to be isotropic and temperature independent, and $A_{\kappa\kappa}^{\mathrm{dip}}$ are the diagonal elements of the dipolar coupling tensor $\mathbf{A}^{\mathrm{dip}}$ with $\Sigma_\kappa A_{\kappa\kappa}^{\mathrm{dip}}=0$. The χ_κ are the components of a local susceptibility tensor $\boldsymbol{\chi}^{\mathrm{loc}}$ which characterizes the magnetic response of the Ce ions in the neighborhood of the μ^+; they are basically responsible for the temperature dependencies of the K_κ components. The K_κ^0 are small T-independent contributions, essentially reflecting the Pauli spin paramagnetism.

It is usually easy to determine the μ^+ site if a scaling of Knight shift with bulk susceptibility is observed, assuming

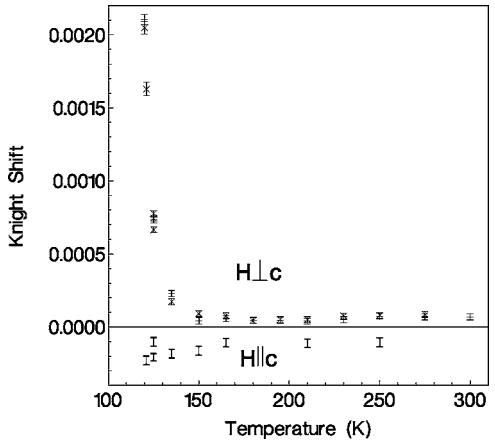

FIG. 2. Temperature dependence of the μ^+ Knight shift for three orientations of the $CeRh_3B_2$ crystal. × for $\boldsymbol{H}\parallel[11\bar{2}0]$ and + for $\boldsymbol{H}\parallel[10\bar{1}0]$ (both with $K_\mu>0$), and I for $\boldsymbol{H}\parallel\boldsymbol{c}$ ($K_c<0$).

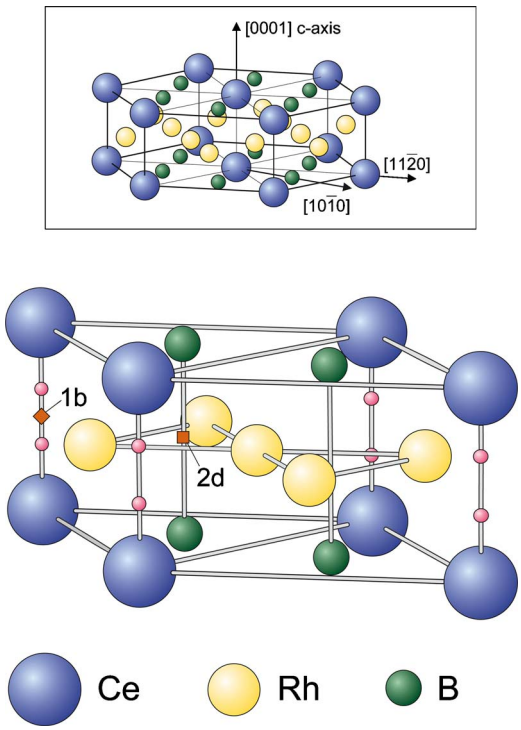

FIG. 3. (Color online) Unit cell of $CeRh_3B_2$, containing one Ce ion at the 1a site, three Rh atoms at the 3g sites, and two B atoms at the 2c sites—the crystallographic axes are specified in the inset. Two μ^+-site candidates are indicated: The 2d site between two B atoms, and the 1b site between two Ce atoms. Magnetic moments are essentially on Ce ions—parallel to the basal plane in the ordered state. A negative magnetic density is possibly found on Rh atoms or delocalized on the [0001] Ce-Ce chains (e.g., around the 2e sites, tiny spheres).

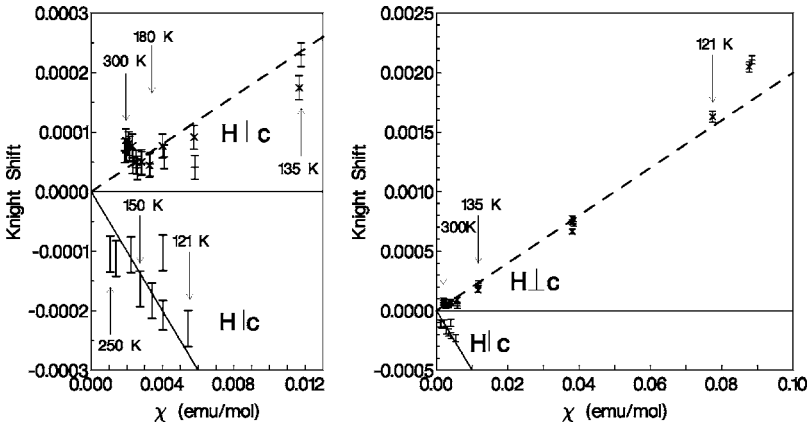

FIG. 4. Muon Knight shift K_μ vs bulk magnetic susceptibility χ (Clogston-Jaccarino plot) for three crystal orientations, $\boldsymbol{H}\|[11\bar{2}0]$ ($\times$) and $\boldsymbol{H}\|[10\bar{1}0]$ (+), both with $K_\mu>0$, and $\boldsymbol{H}\|[0001]$ (I) with $K_c<0$. Right panel: full χ range, left panel: expanded low-χ range. The linear scaling indicated by the dashed and solid straight lines is retained to determine the μ^+ site.

that the *local* susceptibility corresponds to the *bulk* susceptibility. To find out if a scaling relation applies for $CeRh_3B_2$, we have plotted in Fig. 4 the measured μ^+ Knight shifts versus the related bulk susceptibilities (Clogston-Jaccarino plots). For $\boldsymbol{H}$ in the basal plane, a scaling seems effectively verified if one ignores the points close to T_C (see the dashed line). The situation is less clear for $\boldsymbol{H}$ parallel to the c axis. Because of the relatively small Knight shift values, the precision is limited and the data points show a tendency to scatter. Nevertheless, a possible scaling is indicated by the straight solid line in Fig. 4 (assuming also that the line goes through the origin of the axes, i.e., a negligible T-independent contribution to K_c). A significant error has to be retained for the slope $\Delta K_c/\Delta\chi_c$ in order to account for systematic errors in the demagnetization corrections.

For a lattice site with an axially symmetric dipolar field (in the case of $CeRh_3B_2$ the symmetry axis is obviously the c axis) the dipolar tensor is diagonal in the appropriate coordinate system, with its three elements $A_{11}^{\rm dip}$, $A_{22}^{\rm dip}$, $A_{33}^{\rm dip}$ related by $A_{11}^{\rm dip}=A_{22}^{\rm dip}$ and $A_{33}^{\rm dip}=-2A_{11}^{\rm dip}$. In our case $A_{33}^{\rm dip}\equiv A_{cc}^{\rm dip}$, the index c standing for c axis or $[0001]$, and the two other axes being, e.g., $[11\bar{2}0]$ and $[10\bar{1}0]$, with $A_{11}^{\rm dip}$ and $A_{22}^{\rm dip}$ replaced by $A_{bb}^{\rm dip}$, the index b standing for "basal." The dipolar tensor can now be expressed as a function of, e.g., its element $A_{bb}^{\rm dip}$ only. This means Eq. (5) can be rewritten as

$$\Delta K_b/\Delta\chi_b = A^{\rm c} + A_{bb}^{\rm dip}, \tag{6}$$

$$\Delta K_c/\Delta\chi_c = A^{\rm c} + A_{cc}^{\rm dip} = A^{\rm c} - 2A_{bb}^{\rm dip}. \tag{7}$$

The data yield the slopes $\Delta K_b/\Delta\chi_b=0.02$ mol/emu or 0.112 kG/μ_B and $\Delta K_c/\Delta\chi_c=-0.05$ mol/emu or -0.279 kG/μ_B (Fig. 4), from which one readily obtains $A_{bb}^{\rm dip}=0.130(47)$ kG/μ_B and $A^{\rm c}=-0.019(10)$ kG/μ_B. The estimated errors also include the mentioned demagnetization-correction uncertainties.

C. Various solutions for μ^+ sites and magnetic densities in paramagnetic $CeRh_3B_2$

For various crystallographic sites, the dipolar fields are calculated assuming different magnetic moment locations, see Table II. The sites with axially symmetric dipolar fields mentioned above have been retained.

Comparing measurement and calculation, one can, assuming a magnetic density *only on the* Ce *ions*, rule out the μ^+ locations at the 2e sites $(0,0,z)$, between the Ce ions, i.e., also the particular 1b site $(0,0,\frac{1}{2})$. Indeed, for 2e one calculates $A_{bb,2e}^{\rm dip}\leqslant A_{bb,1b}^{\rm dip}=-5.06$ kG/μ_B, far below the value deduced using the Jaccarino plots. On the other hand, for the 2d site, the particular 4h site $(\frac{1}{3},\frac{2}{3},z=\frac{1}{2})$ equidistant between the two B atoms and yielding the smallest absolute $A_{bb}^{\rm dip}$ value, the calculation variant (a) gives $A_{bb,2d}^{\rm dip}=0.184$ kG/μ_B. The small discrepancy with the measured $A_{bb}^{\rm dip}=0.130(47)$ kG/μ_B may arise from other magnetization contributions, as will be discussed now.

So far, following the conclusions of Refs. 2–6, it was assumed that only the Ce ions carry magnetic moments. In fact, a magnetization of the Rh sublattice cannot be entirely excluded. For example, Alonso *et al.* give in their model based refinement analysis an absolute moment of 0.016 μ_B as upper limit on the Rh atom (for a total moment of $\mu_{4f+5d}=0.38$ μ_B/f.u.),[6] and other analyses or measurements forsee far larger magnetic moments on the Rh atoms, with a direction opposed to that of the Ce moments in the ordered state.[7] Looking at Table II, one sees that one can reproduce the measured Knight shift with variant (b), with the μ^+ at the 2d site. In this case one retains, in addition to the magnetization on the Ce atoms [proportional to χ(Ce), the contribution to the total bulk susceptibility stemming from the Ce atoms], a magnetization on the Rh atoms, with antiparallel moments [proportional to χ(Rh), the susceptibility contribution stemming from the Rh atoms]. Here only the ratio of these two susceptibility fractions matters; one obtains the expected total dipolar tensor component $\langle A_{bb}^{\rm dip}\rangle=0.130$ kG/μ_B for the ratio χ(Rh)/χ(Ce)$=-0.061$. The axial symmetry of the dipolar field is conserved. [In this procedure it is implicitly assumed that χ(Rh)/χ(Ce) is independent of T.] This solution, so far, appears plausible. It bears resemblance with the cases of $CeRhIn_5$,[12] and Ce_2RhIn_8,[13] where small negative moments are also induced on the Rh sites.

Another solution [Table II, variant (c)] to reproduce the Knight-shift measurements assumes the μ^+ at the 1b site, the main magnetization at the Ce ions, and a delocalized negative magnetic density along the Ce chain, as, e.g., the μ_{5d} density reported by Alonso *et al.*[6] One has assumed, for the sake of simplicity, the negative magnetization centered on 2e sites. The ratio $\chi(2e)/\chi(Ce)=-0.321$, has been postulated—a value in agreement with the findings of Ref. 6. In

TABLE II. Calculated dipolar fields (tensor component A_{bb}^{dip}) and related parameters for various sites and different magnetic moment locations in $CeRh_3B_2$, with variants labeled in the first column. The sites considered show axially symmetric dipolar tensors ($A_{bb}^{\mathrm{dip}} = -\frac{1}{2}A_{cc}^{\mathrm{dip}}$, b for $\boldsymbol{H} \perp \boldsymbol{c}$, c for $\boldsymbol{H} \| \boldsymbol{c}$). For moments at two different locations n it is now *the ratio* of the values $\chi(n)$, the susceptibility contributions from the Ce ions and from the other location (i.e., Rh or 2e), which matters. This ratio can be tuned to obtain a dipolar-field sum (component denoted $\langle A_{bb}^{\mathrm{dip}} \rangle$) consistent with the Knight shift measurements (last line for comparison). A lattice relaxation around the μ^+ is not considered.

Variant	Site type	Generic co-ord.	Dist. (Å) nearest at. Ce	Rh	B	Moment locat.	A_{bb}^{dip} $\left(\frac{\mathrm{kG}}{\mu_B/\mathrm{atom}}\right)$	Ratio $\frac{\chi(\mathrm{Rh}/2\mathrm{e})}{\chi(\mathrm{Ce})}$	$\langle A_{bb}^{\mathrm{dip}} \rangle$ $\left(\frac{\mathrm{kG}}{\mu_B/\mathrm{f.u.}}\right)$
(a)	2d	$(\frac{1}{3},\frac{2}{3},\frac{1}{2})$	3.52	1.58	1.54	Ce	0.184		0.184
(b)						Ce	0.184	−0.061	0.130
						Rh	2.999		
(d)						Ce	0.184	−0.182	0.168
						2e[a]	0.503		
(c)	1b	$(0,0,\frac{1}{2})$	1.54	2.74	3.52	Ce	−5.063	−0.321	0.130
						2e[b]	−32.070		
(e)						Ce	−5.063	+24.4	0.130
						Rh	1.029		
(f)	6m[c]	$(0.15,0.30,\frac{1}{2})$	2.10	1.67	2.33	Ce	−0.594	+1.34	0.130
						Rh	2.011		
(g)	12p[c]	(0.11,0.35,0)	1.70	1.98	1.55	Ce	0.807	+1.60	0.130
						Rh	−0.882		
—	2c[d]	$(\frac{1}{3},\frac{2}{3},0)$	3.17	2.21	0.0	Ce	0.299		
From μ^+ Knight shift measurement									0.130(47)

[a]Generic co-ord. (0,0,0.275).
[b]Generic co-ord. (0,0,0.225).
[c]With tunneling.
[d]Sites of the B atoms, for comparison.

that case, the measured value $\langle A_{bb}^{\mathrm{dip}} \rangle = 0.130\ \mathrm{kG}/\mu_B$ allows one to determine the exact 2e positions, i.e., generic $(0,0,z_{2e}=0.225)$.

Moreover, variant (d) of Table II, with the μ^+ at 2d and magnetization densities at Ce and 2e sites, also gives a dipolar-tensor value of the expected size. Statistically, the 2d sites are twice as abundant as the 1b sites. On the other hand, variant (e), with the μ^+ at 1b sites and magnetization densities at Ce and Rh sites, gives the expected $\langle A_{bb}^{\mathrm{dip}} \rangle$ only if a very large part of the magnetic density resides on the Rh atoms. Such a drastic change of magnetization location seems unlikely.

Finally, μ^+ locations with axially symmetric dipolar fields can also result from extended localized (or tunneling) states. It has been found, e.g., in UNi_2Al_3,[20] $GdNi_5$,[21] and $DyNi_5$,[22] all compounds with the same $P6/mmm$ space group as $CeRh_3B_2$, that the 6m (or 6k) ring state, around the 1b site, can be populated by a μ^+ at certain temperatures. Each particular site of the ring is not characterized by a uniaxial dipolar field, but due to the extended localization or tunneling of the μ^+ over all ring sites, which results in an averaging, the uniaxial field feature of the extended state is realized. In Table II one has calculated variants (f) and (g), for 6m and 12p tunneling states, respectively. Both examples involve reasonable interstitial free volumes for the μ^+, and through the adequate splitting of the magnetization on Ce and Rh atoms [i.e., by determination of the proper ratio $\chi(\mathrm{Rh})/\chi(\mathrm{Ce})$], again the average $\langle A_{bb}^{\mathrm{dip}} \rangle = 0.130\ \mathrm{kG}/\mu_B$ can be obtained. [The values of the ratio $\chi(\mathrm{Rh})/\chi(\mathrm{Ce})$, rather large in the two examples, could eventually be different, since they are functions of yet incompletely defined ring-site parameters.] However, one has to mention that extended localized or tunneling μ^+ states are not found in all compounds with $P6/mmm$ structure. For instance, in UPd_2Al_3, solely the 1b site is occupied by the muon, see, e.g., Ref. 23.

No lattice relaxation around the μ^+ has been considered in the calculations.

D. Relaxation of the TF signal and simultaneously obtained LF data

In the introduction of Sec. III, the observation of an anisotropic signal relaxation, possibly due to the ^{11}B nuclear moments, has been mentioned. Under this assumption, and placing the μ^+ at the 2d site, one calculates relaxation rates $\sigma = \sqrt{M_2}$ of 0.54 μs^{-1} for $\boldsymbol{H} \| \boldsymbol{c}$ and 0.27 μs^{-1} for $\boldsymbol{H} \perp \boldsymbol{c}$ (in the van Vleck limit). This is in very good agreement with the measurements at 125 K, i.e., 0.55(3) and 0.21(3) μs^{-1}, respectively. Here we have disregarded the effects of the inhomogeneous sample demagnetization fields on M_2, which are not so important for these symmetric sample orientations. Performing the same σ calculations for the μ^+ at the 1b site

or at the 6m tunneling site of Table II one finds, for all Θ values, $\sigma \leqslant 0.1\ \mu s^{-1}$. The relaxation rates σ_κ or λ_κ obtained for $T \gtrsim 125$ K from fits of the TF data first decrease with increasing T. Above ~160 K the relaxation rates for the field parallel to $\boldsymbol{c}$ and perpendicular to $\boldsymbol{c}$ saturate at $\lambda_\kappa \sim 0.03(1)\ \mu s^{-1}$. Therefore, it appears justified to assume that most μ^+ occupy 2d sites at $T \approx 125$ K, at which temperature they start to become mobile (i.e., they diffuse with a jump time $\tau_j \lesssim \tau_\mu$, the muon lifetime).

Alternatively, we have tried to explain the TF signal by the superposition of two (or more) components with unresolved splitting. This was only possible by requiring predefined values or interrelations among some of the signal parameters, since the free fits led in general to inconsistent results. For instance, assuming the contribution of two signals to the angular dependence measured at 125 K and requiring a fixed ratio for the two amplitudes (e.g., 1:1 or 1:4) and a smooth behavior of the relaxation rates, one obtains two distinct frequencies as functions of the crystal orientation in the external field. Compared to the original frequency shift (Fig. 1), the two curves are rather parallel and bracket the one-component signal. All 125 K results together stress the overall uniaxial symmetry property previously retained. We have attempted to extend this procedure to the temperature dependencies measured for the three principal crystal orientations (see Fig. 2). This leads, however, to an increasing number and growing complexity of the assumptions needed and/or to erratic, contradictory, results. This also indicates to us that a one-component signal, i.e., a single μ^+-site occupancy, is the best explanation for the μ^+ in the paramagnetic phase of $CeRh_3B_2$.

As mentioned in Sec. II, simultaneously to the TF data one obtains also LF data by using the F and B positron detectors in the longitudinal field $H_{ext}=6$ kOe. In such a field, the μ^+ spin is decoupled from the static field contributions and the signal reflects only the spin lattice relaxation rate. From 300 K down to T_C, the signals do not reveal any relaxation, i.e., the spin lattice relaxation rates are too slow to be observed within the μSR time window.

IV. ZF MEASUREMENTS

Zero-field μSR measurements have been performed from 5 to 121 K. Two spontaneous precession frequencies, $\nu_i = \omega_i/(2\pi)$, with $i=1,2$, are observed below T_C. Data have mainly been taken with the incident-muon polarization $\boldsymbol{P}_\mu(t=0)$ oriented parallel or perpendicular to the crystallographic c axis, see, e.g., Fig. 5. The μSR signals are best fitted with the sum of two precessing, exponentially damped components, and a nonprecessing term,

$$A_\kappa P_\kappa(t) = A_{0,\kappa} + \sum_{i=1}^{2} A_{i,\kappa} e^{-\lambda_i t} \cos(\omega_i t + \phi), \tag{8}$$

where $\kappa = \parallel$ stands for the orientation with $\boldsymbol{P}_\mu(0) \parallel \boldsymbol{c}$, and $\kappa = \perp$ for $\boldsymbol{P}_\mu(0) \perp \boldsymbol{c}$.

The total initial $A_\kappa P_\kappa(0)$ is known from calibration runs in a small transverse field above T_C. The fits yield $A_{0,\parallel} \approx 0$ for $\boldsymbol{P}_\mu(0) \parallel \boldsymbol{c}$, i.e., $A_{1,\parallel} + A_{2,\parallel} = A_\parallel$, and $A_{0,\perp} \approx 0.4 A_\perp$, with $A_{0,\perp} + A_{1,\perp} + A_{2,\perp} = A_\perp$ for $\boldsymbol{P}_\mu(0) \perp \boldsymbol{c}$. If one assumes that the fields seen by the muons are all in the *ab* plane, but with random orientation for the ensemble (or pseudo-random, i.e., with vector sum zero), ideally one will obtain $A_{i,\perp} = \frac{1}{2} A_{i,\parallel}$, $A_{0,\parallel} = 0$, $A_{0,\perp} = \frac{1}{2}(A_{1,\parallel} + A_{2,\parallel}) = \frac{1}{2} A_{\mathrm{tot}}$. Our observations are basically consistent with such a pattern. The fact that the ratio $A_{0,\perp}/A_\perp$ is not exactly 0.5 might either reveal that the magnetic fields seen by the muons are not strictly parallel to the basal crystallographic plane, but show a narrow orientation distribution, partly out of this plane, or reflect an imperfect determination of the initial $A_\kappa P_\kappa(0)$ values. (The determination of A_κ is not trivial. It necessitates calibration measurements with various fields, configurations, orientations, etc. In particular for small samples, it is tainted with residual uncertainties, the nominal and the calibration measurements being unavoidably performed under slightly different conditions.)

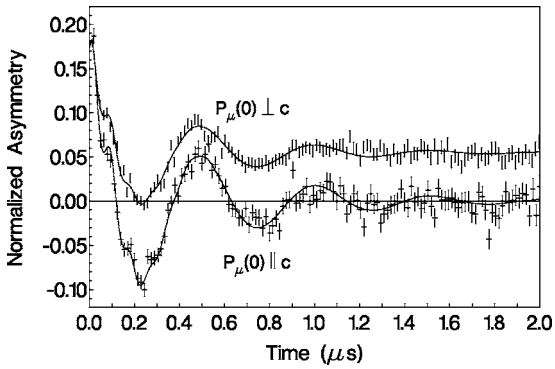

FIG. 5. ZF μSR signals in the "backward" positron detector for $CeRh_3B_2$ at 90 K, with the incident-muon polarization either parallel or perpendicular to the crystallographic c axis. The data are fitted with two frequencies and, for $\boldsymbol{P}_\mu(0) \perp \boldsymbol{c}$, an additional nonprecessing contribution.

The low-frequency signal ν_1 is stronger [with an asymmetry ratio $A_1/A_2 \approx 2.5(3)$, without a clear trend with temperature], and less quickly damped than the high-frequency signal ν_2. The temperature dependencies of ν_i and the corresponding relaxation rates are shown in Fig. 6. Whereas the temperature dependence of ν_2 is conventional, of the Brillouin type, the temperature dependence of ν_1 is peculiar. The frequency is about zero at T_C, climbs rapidly with decreasing temperature to approximately 2 MHz at 90 K, where it peaks, and then decreases smoothly to about 0.8 MHz at 5 K.

Cooke *et al.*[14] have previously performed a crude ZF μSR study on *polycrystalline* $CeRh_3B_2$. They observed only one spontaneous frequency, obviously the lower one. Their four data points, also displayed in Fig. 6, although suggesting a peak in the temperature dependence of the spontaneous frequency, indicate a behavior quite different from our ν_1 data. Let us also mention that in a μSR study with polycrystalline $CeRh_3B_2$ and $Ce(Rh_{1-x}Ru_x)_3B_2$, Reichl has also observed the low- and high-frequency signals.[24] In these measurements, for $CeRh_3B_2$, ν_1 and ν_2 follow only very roughly our single-crystal data. For ν_1, however, the agreement is better than for the data of Cooke *et al.*

Mirroring the variation of T_C reported in Sec. II, a strong sample dependence of the spontaneous μSR frequencies is

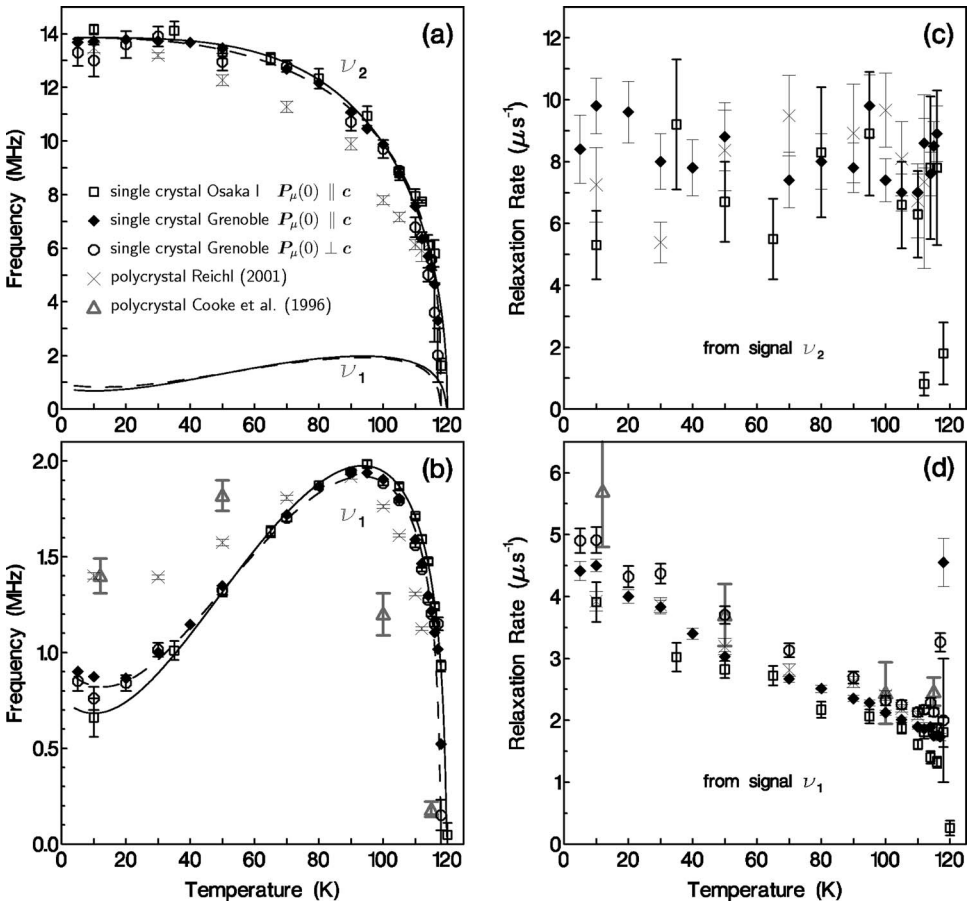

FIG. 6. Temperature dependence of the ZF spontaneous μ^+ precession frequencies ν_2 (a), ν_1 (b), and the related relaxation rates λ or σ (c) and (d) in $CeRh_3B_2$. The solid and dashed curves in (a) and (b) are the mean $\nu(T)$ dependencies assumed for the Osaka and Grenoble single crystals, respectively. The polycrystalline-sample data from Reichl (Ref. 24) and Cooke *et al.* (Ref. 14) are also shown. The symbols used in all panels are explained in (a).

apparent. It should be noted that the fitted frequencies do not depend critically on the assumed relaxation function (Gaussian or experimental), even at the lowest temperatures where ν_1 is much reduced (only about one oscillation period observable). A small difference is visible between the $\nu_i(T)$ data of the Osaka and Grenoble crystals, and even a very slight shift is seen for the two Osaka crystals (all three crystal data fitted the same way—for clarity only the data from one Osaka crystal are shown in Fig. 6). On the other hand, no difference is noticed for the frequencies obtained in each single crystal for different orientations relative to $\boldsymbol{P}_\mu(0)$.

A. Origin of the spontaneous μSR frequencies

In an unmagnetized ferromagnet in ZF the μ^+ precession is governed by the local field at the μ^+, given by[17]

$$\boldsymbol{B}^\mu(\boldsymbol{r}_\mu) = \boldsymbol{B}^{\mathrm{Lor}} + \boldsymbol{B}^{\mathrm{dip}}(\boldsymbol{r}_\mu) + \boldsymbol{B}^c. \tag{9}$$

$\boldsymbol{B}^{\mathrm{Lor}} = (4\pi/3)\boldsymbol{M}$ is the Lorentz field, proportional to the domain magnetization $\boldsymbol{M}$, $\boldsymbol{B}^{\mathrm{dip}}(\boldsymbol{r}_\mu)$ is the lattice sum of the fields of the dipoles inside the Lorentz sphere, and $\boldsymbol{B}^c$ is the contact hyperfine field. The contact-hyperfine coupling $\boldsymbol{B}^c$ is generally isotropic, T-independent and proportional to $\boldsymbol{M}$.

There are two basic mechanisms which can result in *two* spontaneous precession frequencies. First, the crystals might host *two different magnetic domains*. We do not believe this is the case here, since no other empirical fact points to this possibility. Second, two frequencies can be explained if *two different* μ^+ *sites* (at least with respect to the local fields) are occupied. This is incompatible with the single μ^+-site hypothesis discussed in Sec. III (Knight-shift measurements) unless a change in site occupation occurs upon passing from the paramagnetic to the magnetically ordered phase. Obviously, the occurrence of *two* spontaneous precession frequencies rules out the possibility of long-range μ^+ diffusion through the crystal, at least for $T < 117$ K.

In any case, from Fig. 6, one draws the following conclusions:

1. The low-field signal $|B_1^\mu(T)| = (2\pi/\gamma_\mu)|\nu_1(T)|$ can only be explained if there are two field contributions with different temperature dependencies and opposite signs, which tend to cancel as T is lowered towards zero. Obvious sources for these fields are the Ce *and* the Rh ions.

2. The high-field signal $|B_2^\mu(T)|$ at $T=0$ cannot arise solely from the Ce magnetization with μ^+ at 2d sites, since with $B_{bb}^{\mathrm{dip}} = 0.184$ kG/(μ_B/atom), unreasonably large moments at the Ce sites or an unreasonably strong contact hyperfine field would be needed. The "normal" behavior of $|B_2^\mu(T)|$ indicates that at this muon position, the two field sources contribute with rather different strength, such that one contribution clearly dominates.

It should be noted that peculiar behavior of spontaneous precession frequencies similar to the present $\nu_1(T)$ have been observed previously. So, for instance, over a large T range for $(\gamma_\mu/2\pi)B^\mu(T)$ in Gd—see the review in Ref. 17. There, as well as in other similar cases, the explanation lay in a rotation of the easy axis of magnetization relative to the crys-

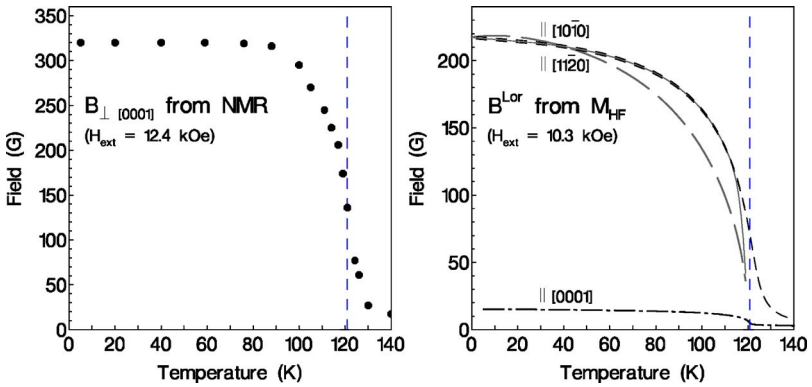

FIG. 7. (Color online) Comparison of $B_\perp(T)$ from nuclear magnetic resonance (NMR) (Ref. 2) left, supposed to be proportional to $|\boldsymbol{M}(T)|$, with $B^{\mathrm{Lor}}(T)=(4\pi/3)M(T)$ from magnetization measurements (Ref. 1), right (two finely dashed curves for $\boldsymbol{H}$ in the ab plane and the dash-dotted curve for $\boldsymbol{H}\|\boldsymbol{c}$). The thin solid curve is the ZF $B^{\mathrm{Lor}}(T)$ as assumed for solutions VD and VM, and the coarsely dashed curve is solution Pd calculated from the μSR frequencies, see Sec. IV C.

tallographic axes. We do not consider this for $CeRh_3B_2$, since no other measurement indicates such a phenomenon, and because the second μ^+ frequency follows a very common T dependence.

B. Framework for a simple model

We proceed now to explain the spontaneous ZF frequencies by a model with two μ^+ sites. Based on the analysis of the Knight-shift data (Table II) and the inferences made in the previous paragraph, we retain the 2d and the 1b sites (in fact the 1b site could be replaced by a 6m-ring state, but the conclusions are not essentially affected; thus, we proceed with the simple 1b-site assumption—the relevant differences for a 6m/1b substitution will be mentioned where necessary). In any case, the recourse to sites with axial field symmetry appears stringent. (For such sites, the calculation of $\boldsymbol{B}^{\mathrm{dip}}$ is simple, essentially being the product of A^{dip}_{bb}, listed in Table II, and the value of the basal-plane moments.) For the magnetic moment locations, we consider both the Ce ions and the Rh atoms. One expects the moments to be aligned in the basal plane, chiefly with the Rh moments parallel or antiparallel to the Ce moments. For each site i, where i stands for either 2d or 1b, $\boldsymbol{B}^{\mathrm{dip}}$ in Eq. (9) can be developed as follows:

$$\boldsymbol{B}^{\mu}_i = \boldsymbol{B}^{\mathrm{Lor}} + \mathbf{A}^{\mathrm{dip}}_{\mathrm{Ce},i}\boldsymbol{m}_{\mathrm{at}}(\mathrm{Ce}) + \mathbf{A}^{\mathrm{dip}}_{\mathrm{Rh},i}\boldsymbol{m}_{\mathrm{at}}(\mathrm{Rh}) + \boldsymbol{B}^{\mathrm{c}}_i. \quad (10)$$

Here the vector $\boldsymbol{m}_{\mathrm{at}}(n)$ is the magnetic moment (in μ_B/atom) at the indicated atom or site (n=Ce,Rh). The dipolar coupling tensor corresponding to such moments is represented for the site i by $\mathbf{A}^{\mathrm{dip}}_{n,i}$, i.e., the related dipolar-field term is $\boldsymbol{B}^{\mathrm{dip}}_{n,i}=\mathbf{A}^{\mathrm{dip}}_{n,i}\boldsymbol{m}_{\mathrm{at}}(n)$. The components of $\mathbf{A}^{\mathrm{dip}}_{n,i}$ are easily calculated; for i=2d and i=1b they are listed in Table II.

The contact hyperfine field contribution $\boldsymbol{B}^{\mathrm{c}}_i$ is governed by the tensor $\mathbf{A}^{\mathrm{c}}_i$, usually assumed to be temperature-independent and isotropic, i.e., it reduces to the scalar A^{c}_i.[18] (From the analysis of Sec. III B, we infer that A^{c} is small and possibly zero for the paramagnetic state.) For an isotropic $\mathbf{A}^{\mathrm{c}}_i$, the contact field $\boldsymbol{B}^{\mathrm{c}}_i$ can be written by introducing, without loss of generality, scalar contact-term coefficients $b^{\mathrm{c}}_{n,i}$:

$$\boldsymbol{B}^{\mathrm{c}}_i = b^{\mathrm{c}}_{\mathrm{Ce},i}\boldsymbol{m}_{\mathrm{at}}(\mathrm{Ce}) + b^{\mathrm{c}}_{\mathrm{Rh},i}\boldsymbol{m}_{\mathrm{at}}(\mathrm{Rh}). \quad (11)$$

This expresses the fact that $\boldsymbol{B}^{\mathrm{c}}_i$ is proportional to the two "primary" sources of magnetization. [In that sense a possible magnetization at the 2e sites, $\boldsymbol{m}_{\mathrm{at}}(2\mathrm{e})$, would be an induced "secondary" Ce magnetization; it is not necessary to introduce it explicitly here, since, if required, the contribution of such a magnetization density may be absorbed into the $b^{\mathrm{c}}_{\mathrm{Ce},i}$ terms. Since the exchange coupling between the 5d and 4f Ce states is independent of temperature, the ratio $m_{\mathrm{at}}(2\mathrm{e})/m_{\mathrm{at}}(\mathrm{Ce})$ would also remain constant.] We may now reformulate Eq. (10):

$$\boldsymbol{B}^{\mu}_i = \boldsymbol{B}^{\mathrm{Lor}} + (\mathbf{A}^{\mathrm{dip}}_{\mathrm{Ce},i} + b^{\mathrm{c}}_{\mathrm{Ce},i})\boldsymbol{m}_{\mathrm{at}}(\mathrm{Ce}) + (\mathbf{A}^{\mathrm{dip}}_{\mathrm{Rh},i} + b^{\mathrm{c}}_{\mathrm{Rh},i})\boldsymbol{m}_{\mathrm{at}}(\mathrm{Rh}). \quad (12)$$

Each of the four $b^{\mathrm{c}}_{n,i}$ is taken to be constant.

The total magnetic moment per formula unit $\boldsymbol{m}^{\mathrm{tot}}_{\mathrm{fu}}$ is obtained by summing over the moments $\boldsymbol{m}_{\mathrm{at}}(n)$, taking account of site multiplicities:

$$\boldsymbol{m}^{\mathrm{tot}}_{\mathrm{fu}} = \boldsymbol{m}_{\mathrm{at}}(\mathrm{Ce}) + 3\boldsymbol{m}_{\mathrm{at}}(\mathrm{Rh}). \quad (13)$$

$\boldsymbol{m}^{\mathrm{tot}}_{\mathrm{fu}}$, a function of T, corresponds to the domain magnetization $\boldsymbol{M}$:

$$\boldsymbol{M}(T) = \frac{\mu_B}{V_{\mathrm{fu}}}\boldsymbol{m}^{\mathrm{tot}}_{\mathrm{fu}}(T), \quad (14)$$

with V_{fu} the volume of the formula unit. For $CeRh_3B_2$, one has μ_B/V_{fu}=115.35 G/(μ_B/f.u.). Information on $M(T)$ is available, e.g., from NMR data[2] or from magnetization measurements with a superconducting quantum interference device (SQUID) magnetometer,[1,25] both of which measurements were performed in an external field (12.4 and 10.3 kOe, respectively). In Fig. 7, we compare the two data sets.

For the analysis of our μSR frequencies, we begin with the magnetization based on the SQUID measurements. Since these data were not obtained in zero field, we consider only the low-temperature range of the relevant data, obtained with fields perpendicular to the c axis, and take an average for the (negligible) difference of the two orientations $\boldsymbol{H}\|[10\bar{1}0]$ and $\boldsymbol{H}\|[11\bar{2}0]$; we denote the average high-field magnetization for $\boldsymbol{H}$ in the basal plane by $M_{\mathrm{HF}}(T)$. The value of the saturation magnetic moment, 0.45 μ_B/f.u., is assumed to be independent of the external field, and hence also applicable for ZF. The temperature dependence of the ZF magnetization, M_{ZF}, is expected to follow $M_{\mathrm{HF}}(T)$ at low temperature, but eventually it should deviate and tend towards zero at T_C. A tentative assumption for $M_{\mathrm{ZF}}(T)$, shown, e.g., in Fig. 7 and as solution VD of Fig. 8, has been used for an initial calculation, see Sec. IV C.

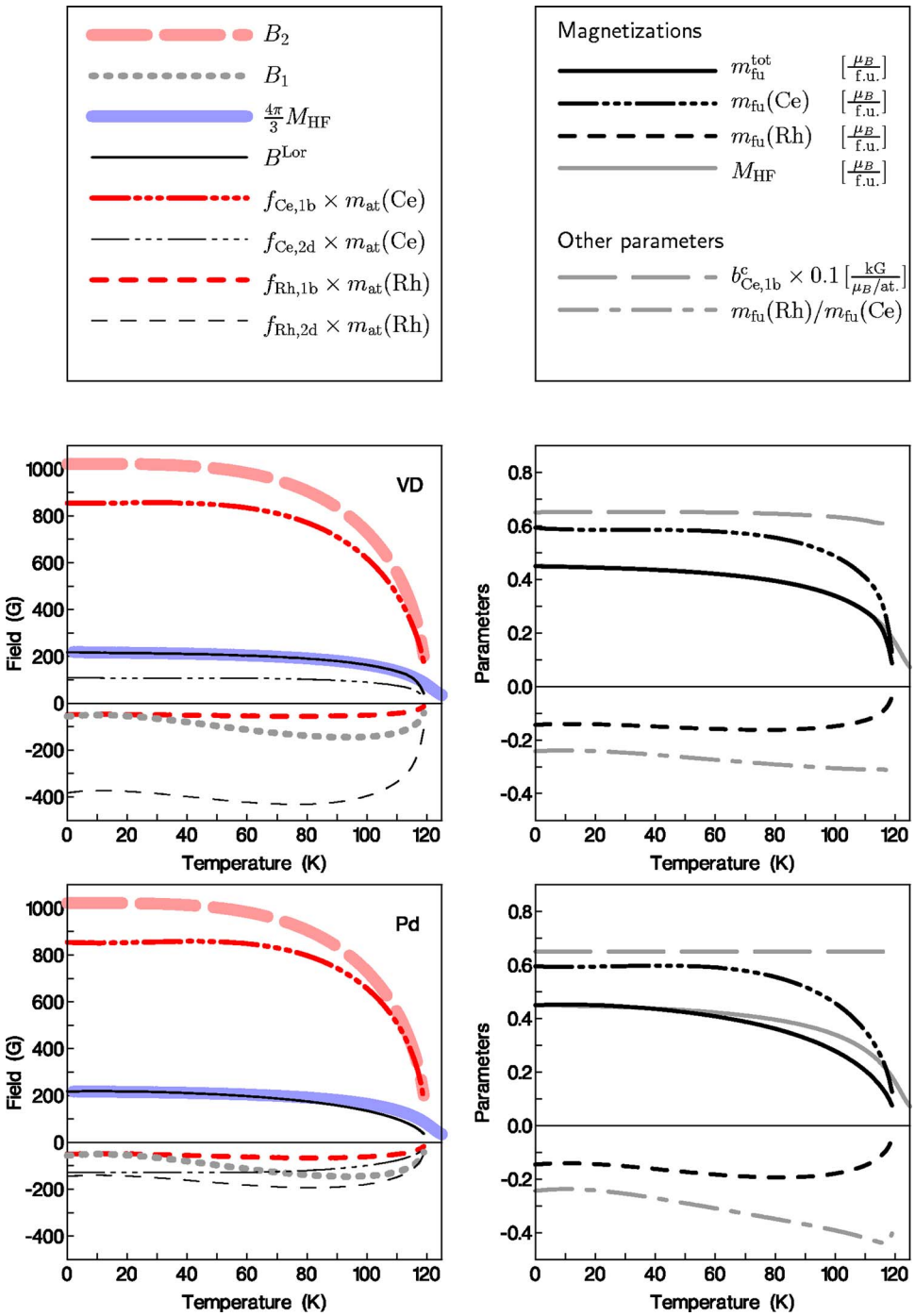

FIG. 8. (Color online) Field contributions to B_1^μ and B_2^μ [Eqs. (16) and (17)] and magnetization parameters from solutions VD and Pd (Table III) in ferromagnetic $CeRh_3B_2$ (labels in the upper right corner of the field panels, lines explained in the top panels). $f_{n,i}=(A_{n,i}^{\rm dip}+b_{n,i}^{\rm c})$ for n=Ce,Rh and i=1b,2d.

Equation (12) implies that all field and magnetic-moment vectors [Eqs. (9)–(14)] *are co-linear*, in the *ab* plane, parallel to the spontaneously ordered moments. The equations now deal exclusively with scalar entities, such as the components along the spontaneous magnetization direction of the Ce moments. In Eq. (10), only the terms $A_{bb}^{\rm dip}$ of the dipolar tensors, discussed in Sec. III C, are needed. We require that the measured dependencies $\pm(2\pi/\gamma_\mu)\nu_1(T)$ and $\pm(2\pi/\gamma_\mu)\nu_2(T)$ are given by the local fields $B_{\rm 2d}^\mu$ and $B_{\rm 1b}^\mu$, calculated with Eqs. (12)–(14)—the signs of the two fields relative to $M_{\rm ZF}$ and the order of their assignment to the two frequencies are *a priori* unknown.

C. Calculation scheme and possible solutions

Without *a priori* assumptions, an infinite number of solutions is evidently possible for the sets of T-dependent $m_{\rm at}(n)$ and the $b_{n,i}^{\rm c}$ parameters. Most of these solutions are meaningless, either because they involve nonphysical parameter values, or because they lead to contradictions with the measurement or with the stated assumptions. We now proceed to extract a few possible solution sets by introducing realistic constraints.

Explicitly, for each temperature point, one deals with a system of three equations,

TABLE III. Sets of input parameters and results at $T \to 0$, corresponding to model calculations; the T dependencies for the last four sets are shown in Figs. 8 and 9. The first column gives the label identifying the set.

Set label	B_1^μ sign[a]	B_2^μ sign[a]	$b^c_{Ce,1b}$ $\left(\frac{kG}{\mu_B/at.}\right)$	$b^c_{Ce,2d}$ $\left(\frac{kG}{\mu_B/at.}\right)$	$b^c_{Rh,1b}$ $\left(\frac{kG}{\mu_B/at.}\right)$	$b^c_{Rh,2d}$ $\left(\frac{kG}{\mu_B/at.}\right)$	B^{Lor} $(T>0)$	$m_{fu}(Ce)$ $\left(\frac{\mu_B}{f.u.}\right)$	$m_{fu}(Rh)$ $\left(\frac{\mu_B}{f.u.}\right)$
Vh	+	−	1.738	−0.79	0	0	calc.	0.380	+0.070
Vn	+	−	2.864	0	0	5.0	calc.	0.548	−0.098
Vj	−	−	3.834	0	0	0	calc.	0.887	−0.437
Vg	−	+	6.851	−0.79	0	0	calc.	0.450	0
Vl	+	+	6.274	0	0	0	calc.	0.749	−0.299
Vf	+	+	7.069	0	8.0	5.0	calc.	0.548	−0.098
Vd	−	+	6.501	0	0	5.0	calc.	0.593	−0.143
VD	−	+	(6.501)	0	0	5.0	entered	0.593	−0.143
Pd	−	+	6.498	−0.40	0	0	calc.	0.595	−0.145
VM	+	+	(6.274)	0	0	0	entered	0.749	−0.299
Pe	+	+	6.487	−0.20	0	0	calc.	0.601	−0.151

[a]Sign relative to B^{Lor}.

$$B^{Lor}(T) = \frac{4\pi}{3}\frac{\mu_B}{V_{fu}}[m_{at}(Ce,T) + 3m_{at}(Rh,T)], \quad (15)$$

$$\text{sign}_1 \times |B_1^\mu(T)| = B^{Lor}(T) + (A^{dip}_{Ce,j} + b^c_{Ce,j})m_{at}(Ce,T) + (A^{dip}_{Rh,j} + b^c_{Rh,j})m_{at}(Rh,T), \quad (16)$$

$$\text{sign}_2 \times |B_2^\mu(T)| = B^{Lor}(T) + (A^{dip}_{Ce,k} + b^c_{Ce,k})m_{at}(Ce,T) + (A^{dip}_{Rh,k} + b^c_{Rh,k})m_{at}(Rh,T), \quad (17)$$

which relate (without considering other constraints) the temperature dependencies of $B^{Lor}(T>0)$ [$B^{Lor}(T=0)$ is known], $m_{at}(Ce,T)$, $m_{at}(Rh,T)$, and the four parameters $b^c_{Ce,j}$, $b^c_{Rh,j}$, $b^c_{Ce,k}$, $b^c_{Rh,k}$. In addition, sign_1, sign_2 and the assignment $(j,k)=(2d,1b)$ or (1b,2d) have to be determined.

The dipole-tensor components $A^{dip}_{n,i}$ are readily computable constants. The absolute values of the fields B_1^μ and B_2^μ are taken from the spontaneous μSR frequencies ν_1 and ν_2—for the calculation we use as T dependencies the parametrized curves describing the Osaka-crystal data, which are shown in Figs. 6(a) and 6(b).

Judging from the values of the dipolar components $A^{dip}_{n,i}$, the assumption that the μ^+ at the 2d sites experiences the small internal field (B_1) and the μ^+ at the 1b sites experiences the large internal field (B_2) is compelling. Hence ν_1 stems from μ^+ at the 2d sites, and ν_2 from μ^+ at the 1b sites.

For a first trial calculation, one enters the assumed $B^{Lor}(T)$ function [i.e., $m^{tot}_{fu}(T)$!], selects the two field signs, and enters three of the contact-field coefficients. Resolving for each T point the equation systems (15)–(17), one obtains the T-dependent split of $m^{tot}_{fu}(T)$ into $m_{fu}(Ce)[=m_{at}(Ce)]$ and $m_{fu}(Rh)[=3m_{at}(Rh)]$, and the fourth contact-field coefficient. Proceeding this way, one deals with an over-determined system, and the fourth contact-field coefficient is not a constant, but shows a (generally weak) T-dependence. Examination of the results (as shown, e.g., for solutions VD and VM, in Table III and Figs. 8 and 9) allows us to discard improper parameter assignments and facilitates the second stage of calculation.

In this second calculation, guided by the previous results, one enters the sign assignments for B_1 and B_2, and all four (constant) contact-field parameters. B^{Lor} for $T>0$ no longer needs to be specified; the calculation now yields the temperature dependence of the Lorentz field—i.e., the full $m^{tot}_{fu}(T)$—together with the split into $m_{fu}(Ce,T)$ and $m_{fu}(Rh,T)$. The examination of these three functions allows us to validate or reject the chosen input parameters.

Numerous calculations with different input-parameter sets have been performed. A summary of selected results is presented in Table III.

Two examples of plausible solutions, labeled Pd and Pe, are shown in Table III and Figs. 8 and 9, together with the corresponding solutions of the first trial calculation, VD and VM.

Compared with the normalized high-field magnetization $(4\pi/3)M_{HF}$, the obtained $B^{Lor}(T)$ shows for Pd (− for sign_1, + for sign_2) a slight under-shoot around 60–90 K, and for Pe (+ for sign_1 and sign_2) a slight over-shoot in the same T range. For both cases, the behavior is compatible with what one expects for $(4\pi/3)M_{ZF}$ and does not by itself allow a choice among the cases. This slight under- or over-shoot feature is characteristic for all reasonable solutions. On the other hand, compared to $(4\pi/3)M_{HF}$, one obtains for $B^{Lor}(T)$ with the assignment $(\text{sign}_1,\text{sign}_2)=(-,-)$ a strong, unacceptable under-shoot, and with the assignment $(\text{sign}_1,\text{sign}_2)=(+,-)$ an unacceptable over-shoot for $T>40$ K.

V. DISCUSSION

The various parameter sets in Table III present solutions for the $CeRh_3B_2$ magnetization below T_C which explain the

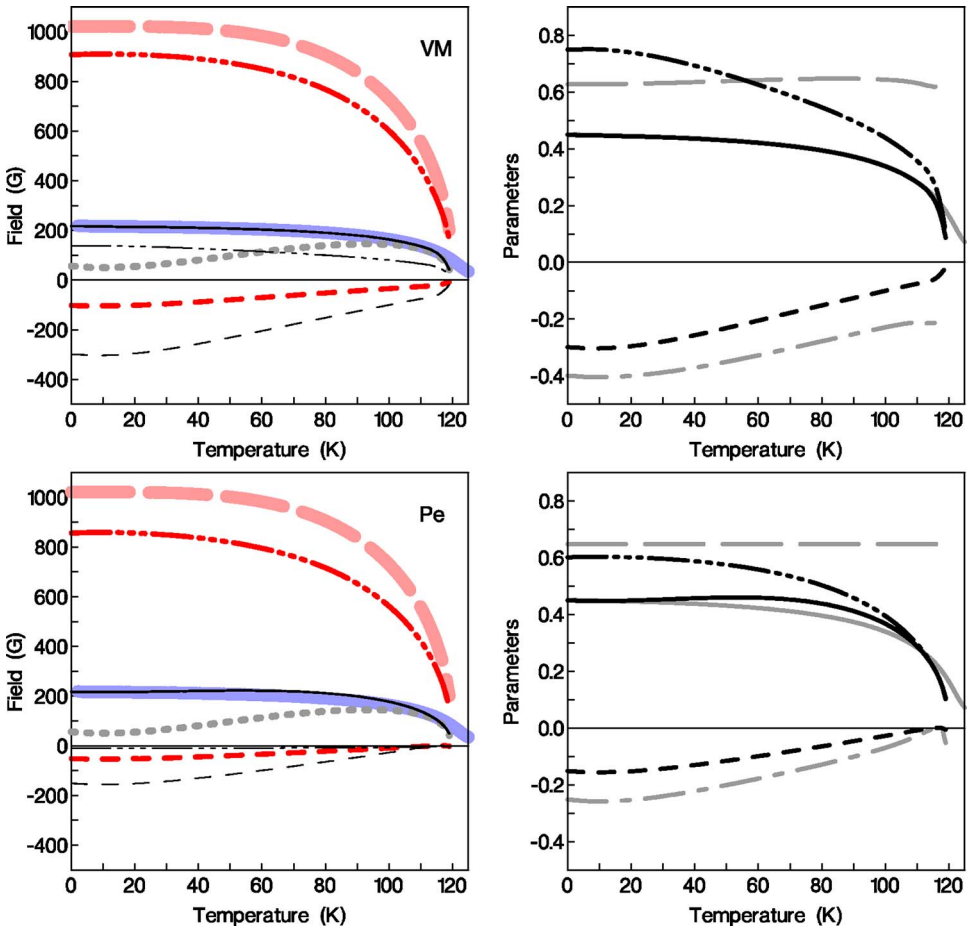

FIG. 9. (Color online) Fields and magnetization parameters from solutions VM and Pe. For explanation, see Fig. 8.

spontaneous ZF μSR signals and contain elements to describe other features of the data, from TF μSR as well as from polarized neutron scattering, etc. So far, however, none of these solutions is consistent with *all* reported findings. Either certain experiments were imperfectly analyzed, or not all of the numerous, particular cases allowed by the model have been comprehensively tested. Nevertheless, the aforementioned solutions allow us to draw some general conclusions.

The difference in the normalized temperature dependencies of B_1^μ and B_2^μ follows from the difference between the functions $|m_{\mathrm{fu}}(\mathrm{Ce},T)|$ and $|m_{\mathrm{fu}}(\mathrm{Rh},T)|$. More specifically, the ratio $m_{\mathrm{fu}}(\mathrm{Rh})/m_{\mathrm{fu}}(\mathrm{Ce})$ (Figs. 8 and 9) either decreases or increases with increasing temperature (for most cases and temperature ranges, the ratio is negative).

Acceptable solutions [i.e., with a reasonable $B^{\mathrm{Lor}}(T)$ behavior and not too large $|m_{\mathrm{fu}}(\mathrm{Rh})|$ values] can be obtained with small or zero values for $b^{\mathrm{c}}_{\mathrm{Rh,1b}}$ and $b^{\mathrm{c}}_{\mathrm{Rh,2d}}$. On the other hand, $b^{\mathrm{c}}_{\mathrm{Ce,1b}}$ must stay within the range $\sim$6 to 7 kG/(μ_B/at.). The importance of this finding must be stressed. As mentioned in Sec. IV B, it points to the existence of an induced magnetization contribution connected to the Ce atoms, located on the *c* axis *between* these atoms, e.g., centered on 2e sites. If one substitutes the 1b μ^+ site by a 6m-ring state, one essentially obtains the same picture, except that $b^{\mathrm{c}}_{\mathrm{Ce,6m}}$, corresponding to $b^{\mathrm{c}}_{\mathrm{Ce,1b}}$, is reduced to approximately 2 kG/(μ_B/at.). The previous indication of 2e moments remains valid.

The $b^{\mathrm{c}}_{\mathrm{Ce,2d}}$ parameter is generally close to zero. If one decreases its value, typically in the range 0 to -1 kG/(μ_B/at.), one reduces the absolute value of the negative $m_{\mathrm{fu}}(\mathrm{Rh})$. In fact, one can achieve a $m_{\mathrm{fu}}(\mathrm{Rh})$ value which crosses zero at a certain temperature, eventually becoming positive. This behavior, although unusual for a sublattice magnetization, could explain the small or nonexistent Rh magnetization reported by the neutron scattering measurements at 7 K.

Solution Vg is characterized by a negligible $m_{\mathrm{fu}}(\mathrm{Rh})$ below $\sim$30 K. This would be consistent with the neutron-scattering study.[6] The Rh moments $|m_{\mathrm{fu}}(\mathrm{Rh})|$ develop only at higher T. However, as for solution Pd, the extrapolated mean values $\langle A^{\mathrm{dip}}_{bb,i}+b^{\mathrm{c}}_i\rangle$, which reflect the average weighted Ce and Rh magnetization sources, extrapolated to $\sim$125 K, amount to $\langle A^{\mathrm{dip}}_{bb,\mathrm{2d}}+b^{\mathrm{c}}_{\mathrm{2d}}\rangle \approx -1.2$ kG/(μ_B/f.u.) and $\langle A^{\mathrm{dip}}_{bb,\mathrm{1b}}+b^{\mathrm{c}}_{\mathrm{1b}}\rangle \approx 2.3$ kG/(μ_B/f.u.). For both muon sites, these values are incompatible with the Knight-shift data.

For solutions Vl and Pe, on the other hand, one finds noticeable Rh moments at low T, and the ratio $|m_{\mathrm{fu}}(\mathrm{Rh})/m_{\mathrm{fu}}(\mathrm{Ce})|$ decreases with increasing temperature. For the 2d muon site, it leads to $\langle A^{\mathrm{dip}}_{bb,\mathrm{2d}}+b^{\mathrm{c}}_{\mathrm{2d}}\rangle \approx -0.1$ kG/(μ_B/f.u.), consistent with the Knight-shift measurements. Since for the 1b sites, one obtains $\langle A^{\mathrm{dip}}_{bb,\mathrm{1b}}+b^{\mathrm{c}}_{\mathrm{1b}}\rangle \approx 1.4$ kG/(μ_B/f.u.), i.e., approximately 10 times the measured value, it implies that no μ^+ reside at 1b sites in the paramagnetic phase. Solution Vf is similar to Vl, although with slightly smaller $|m_{\mathrm{fu}}(\mathrm{Ce})|$ and $|m_{\mathrm{fu}}(\mathrm{Rh})|$ moments. However,

for Vf one obtains large values of $b^c_{Rh,1b}$ and $b^c_{Rh,2d}$.

In all cases, it is necessary to allow for an unusual temperature dependence of $|m_{fu}(Rh)|$, deviating significantly from $|m_{fu}(Ce)|$. This points to a strong temperature dependent exchange coupling between the Ce and Rh $4f$ and $4d$ states, which might be related to the unusual c/a behavior in the crystal. In Ref. 25, one finds a compilation and/or measurements of the temperature dependence of the lattice parameters in $Ce(Rh_{1-x}Ru_x)_3B_2$ for $0 \leqslant x \leqslant 0.4$. In $CeRh_3B_2$, for T decreasing from 300 K to $T_C \approx 120$ K, one observes a strong monotonic decrease of the c parameter by $\sim -0.9\%$. Lowering further the temperature, the variation of $\Delta c/c$ diminishes, so that between 50 and 3.5 K c stays approximately constant at $\sim 99.0\%$ of its value at 300 K. This temperature dependence is smooth, without marked discontinuities. The T dependence of $\Delta a/a$ is similar, however in the opposite direction and less dramatic. At low T, a amounts to $\sim 100.2\%$ of its value at 300 K. The variation below T_C of the highly anisotropic unit cell dimensions is explained by magnetostriction effects. A Ru/Rh substitution significantly diminishes the cell variation, as it also drastically reduces the ordering temperature. It is, therefore, plausible that these variations involve an effect on the exchange coupling between the Ce and Rh electronic states.

The strong exchange coupling of the Ce and Rh moments may also point to rather delocalized $4f$ and $4d$ states, supporting the assignment of $CeRh_3B_2$ as an itinerant magnet. The latter may explain the unusually high Curie temperature T_C, as mentioned in Sec. I.

Let us briefly add that we have also extended the model, allowing an additional magnetization density to build up on the 2e sites. With the exception of a clear indication of a 2e magnetization *antiparallel* to the Ce magnetization, no new basic features appear. As expected, all results are encompassed in the previously presented solutions.

VI. SUMMARY

The observation in the paramagnetic phase of $CeRh_3B_2$ of a single-component μ^+ Knight-shift signal indicates that above 125 K the μ^+ occupies only a single site with axial symmetry, identified as the 2d site. From the scaling of the Knight shift with the bulk susceptibility, one can determine the dipolar-coupling and contact-coupling parameters for the muon locations in that temperature range. Only the 2d sites are compatible with both the Knight shift and the signal relaxation rate σ.

In the magnetically ordered state of $CeRh_3B_2$, two spontaneous μ^+-precession frequencies are observed. It indicates that below 117 K, the two sites 2d and 1b (or 6m ring) are simultaneously occupied by the μ^+, with approximately 2.5 times more muons at the 2d than at the 1b sites. Analogous to the variation of T_C, a sample dependent variation of the two frequencies is noticed.

Based on the temperature dependence of the spontaneous frequencies, our analysis yields the T dependence (for $T > 0$) of the total ZF magnetization, and indicates how it splits into various sublattice components. It shows that a magnetization is found on both Ce *and* Rh atoms. However, it does not exclude that the Rh magnetization disappears for a part of the temperature range below T_C. A polarized neutron study (at 7 K) is incompatible with the presence of magnetization on the Rh sites.[6] We believe that comprehensive neutron scattering measurements over the entire temperature range should allow one to determine the T-dependence of the Rh-magnetization component.

On the other hand, we have a strong indication that a non-negligible negative fraction of the magnetization connected to the Ce atoms is delocalized on the [0001] Ce-Ce chains, e.g., around 2e sites, as also proposed by the neutron study.

The analysis necessitates an unusual temperature dependence of $|m_{fu}(Rh)|$, deviating significantly from $|m_{fu}(Ce)|$. This points to a temperature dependent exchange coupling between the Ce and Rh $4f$ and $4d$ states.

The difference in site population behavior above and below T_C (more precisely, below 117 K and above 125 K, as evidenced by the data) points to static, immobile μ^+ below 117 K and fast long-range diffusion above 125 K.

ACKNOWLEDGMENTS

We wish to thank the Laboratory for Muon-Spin Spectroscopy (LMU), in particular the teams of the Dolly and GPS instruments, and the proton accelerator crew of the Paul Scherrer Institut (PSI) for providing excellent measuring conditions. We are grateful to P. Dalmas de Réotier (CEA Grenoble) for expert advice and stimulating discussions. Finally, we thank P. Lejay (CEA Grenoble) and P. Dalmas de Réotier for allowing us to use their single crystal sample, and B. D. Patterson (PSI) for careful reading of the manuscript.

*Present address: Arsenal Research, Business Unit Transport Technologies, A-1210 Vienna, Austria.

[1] A. Galatanu, E. Yamamoto, T. Okubo, M. Yamada, A. Thamizhavel, T. Takeuchi, K. Sugiyama, Y. Inada, and Y. Ōnuki, J. Phys.: Condens. Matter **15**, S2187 (2003).

[2] Y. Kitaoka, Y. Kishimoto, K. Asayama, T. Kohara, K. Takeda, R. Vijayaraghavan, S. K. Malik, S. K. Dhar, and D. Rambabu, J. Magn. Magn. Mater. **52**, 449 (1985).

[3] A. Fujimori, T. Takahashi, A. Okabe, M. Kasaya, and T. Kasuya, Phys. Rev. B **41**, 6783 (1990).

[4] J. Ph. Schillé, F. Bertran, M. Finazzi, Ch. Brouder, J. P. Kappler, and G. Krill, Phys. Rev. B **50**, 2985 (1994).

[5] S. A. Shaheen, J. S. Schilling, and R. N. Shelton, Phys. Rev. B **31**, 656 (1985).

[6] J. A. Alonso, J. X. Boucherle, F. Givord, J. Schweizer, B. Gillon, and P. Lejay, J. Magn. Magn. Mater. **177-181**, 1048 (1998).

[7] T. Kasuya, K. Takegahara, N. Kobayashi, M. Kasaya, and A. Okabe, in *Theoretical and Experimental Aspects of Valence*

Fluctuations and Heavy Fermions, edited by L. C. Gupta and S. K. Malik (Plenum, New York, 1987), p. 187.

[8] A. Yaouanc, P. Dalmas de Réotier, J.-P. Sanchez, Th. Tschentscher, and P. Lejay, Phys. Rev. B **57**, R681 (1998).

[9] Y. Sakurai, M. Itou, J. Tamura, S. Nanao, A. Thamizhavel, Y. Inada, A. Galatanu, E. Yamamoto, and Y. Ōnuki, J. Phys.: Condens. Matter **15**, S2183 (2003).

[10] T. Okubo, M. Yamada, A. Thamizhavel, S. Kirita, Y. Inada, R. Settai, H. Harima, K. Takegahara, A. Galatanu, E. Yamamoto, and Y. Ōnuki, J. Phys.: Condens. Matter **15**, L721 (2003).

[11] M. Yamada, Y. Obiraki, T. Okubo, T. Shiromoto, Y. Kida, M. Shiimoto, H. Kohara, T. Yamamoto, D. Honda, A. Galatanu, Y. Haga, T. Takeushi, K. Sugiyama, R. Settai, K. Kindo, S. K. Dhar, H. Harima, and Y. Ōnuki, J. Phys. Soc. Jpn. **73**, 2266 (2004).

[12] A. Schenck, D. Andreica, F. N. Gygax, D. Aoki, and Y. Ōnuki, Phys. Rev. B **66**, 144404 (2002).

[13] A. Schenck, F. N. Gygax, T. Ueda, and Y. Ōnuki, Phys. Rev. B **70**, 054415 (2004).

[14] D. W. Cooke, B. L. Bennett, A. C. Lawson, J. G. Huber, J. Oostens, C. Boekema, J. A. Flint, and R. L. Lichti, Philos. Mag. B **74**, 259 (1996).

[15] Homepage of the Laboratory for Muon Spectroscopy of PSI, http://lmu.web.psi.ch

[16] M. Kasaya, A. Okabe, T. Takahashi, T. Satoh, T. Kasuya, and A. Fujimori, J. Magn. Magn. Mater. **76 and 77**, 347 (1988).

[17] A. Schenck and F. N. Gygax, in *Handbook of Magnetic Materials*, edited by K. H. J. Buschow (Elsevier, Amsterdam, 1995), Vol. 9, p. 57.

[18] A. Schenck, in *Muon Science*, edited by S. L. Lee, S. H. Kilcoyne, and R. Cywinsky (SUSSP Publications and Institute of Physics Publishing, Bristol, 1999), p. 39.

[19] P. G. Akishin and I. A. Gaganov, J. Magn. Magn. Mater. **110**, 175 (1992).

[20] A. Schenck, N. K. Sato, G. Solt, D. Andreica, F. N. Gygax, M. Pinkpank, and A. Amato, Eur. Phys. J. B **13**, 245 (2000).

[21] A. M. Mulders, P. C. M. Gubbens, C. T. Kaiser, A. Amato, F. N. Gygax, A. Schenck, P. Dalmas de Réotier, A. Yaouanc, K. H. J. Buschow, F. Kayzel, and A. A. Menovsky, J. Alloys Compd. **330-332**, 454 (2002).

[22] A. M. Mulders, C. T. Kaiser, S. J. Harker, P. C. M. Gubbens, A. Amato, F. N. Gygax, A. Schenck, P. Dalmas de Réotier, A. Yaouanc, K. H. J. Buschow, and A. A. Menovsky, Phys. Rev. B **67**, 014303 (2003).

[23] A. Amato, Rev. Mod. Phys. **69**, 1119 (1997).

[24] Ch. Reichl, Thesis, Vienna University of Technology (2001, unpublished).

[25] St. Berger, A. Galatanu, G. Hilscher, H. Michor, Ch. Paul, E. Bauer, P. Rogl, M. Gómez-Berisso, P. Pedrazzini, J. G. Sereni, J. P. Kappler, A. Rogalev, S. Matar, F. Weill, B. Chevalier, and J. Etourneau, Phys. Rev. B **64**, 134404 (2001).